UNIVERSITÉ DE GENÈVE

Archive ouverte UNIGE
https://archive-ouverte.unige.ch

Article scientifique | Article | 2011

Published version | Open Access

This is the published version of the publication, made available in accordance with the publisher's policy.

Quantitative techniques in PET-CT imaging

Zaidi, Habib; Basu, Sandip; Holm, Soren; Alavi, Abass

How to cite

ZAIDI, Habib et al. Quantitative techniques in PET-CT imaging. In: Current medical imaging reviews, 2011, vol. 7, n° 3, p. 216–233. doi: 10.2174/157340511796411186

This publication URL: https://archive-ouverte.unige.ch/unige:30794
Publication DOI: 10.2174/157340511796411186

© This document is protected by copyright. Please refer to copyright holder(s) for terms of use.

Quantitative Techniques in PET-CT Imaging

Sandip Basu[1], Habib Zaidi[2,3,4], Søren Holm[5] and Abass Alavi[6,*]

[1]*Radiation Medicine Centre (BARC), Tata Memorial Hospital Annexe, Jerbai Wadia Road, Parel, Bombay 400 012, India*

[2]*Division of Nuclear Medicine and Molecular Imaging, Geneva University Hospital, 1211 Geneva, Switzerland*

[3]*Geneva Neuroscience Center, Geneva University, CH-1211 Geneva, Switzerland*

[4]*Department of Nuclear Medicine and Molecular Imaging, University Medical Center Gronigen, University of Groningen, 9700 RB Groningen, Netherlands*

[5]*Clinic of Nuclear Medicine and PET, Rigshospitalet, University of Copenhagen, Denmark*

[6]*Division of Nuclear Medicine, Hospital of the University of Pennsylvania, Philadelphia, PA, USA*

Abstract: The appearance of hybrid PET/CT scanners has made quantitative whole body scanning of radioactive tracers feasible. This paper deals with the novel concepts for assessing global organ function and disease activity based on combined functional (PET) and structural (CT or MR) imaging techniques, their advantages over current quantitative techniques and their potential clinical applications in the management of various diseases. First the complicated kinetic modeling and methods for calculation of the standardized uptake value (SUV) that have been utilized in the practice of clinical PET are briefly described. Subsequently we discuss the quantitative concepts in PET-CT imaging that have been developed in recent years: (a) SUV analysis in the dual-time point and delayed PET imaging, (b) partial volume correction of SUV for small lesions (c) assessment of global metabolic activity in the whole organ or of diseased sites and (d) the novel image segmentation techniques with FDG-PET and newer tracers to precisely define the diseased or intended normal tissue which is of great value for image guided radiation therapy.

Keywords: Hybrid imaging, positron emission tomography (PET), quantitative imaging, standardized uptake value (SUV).

1. INTRODUCTION

In this review, we describe the existing and evolving quantitative approaches in positron emission tomography (PET)/Computed Tomography (PET-CT) imaging that may allow accurate assessment of global and regional function by utilizing the modern tomographic imaging modalities. In order to provide quantitative results in PET, a correction for physical degrading factors including tissue attenuation of the annihilation photons, Compton scatter and detection of random events is necessary. For brain studies this might to a reasonably accuracy be performed by pure calculation assuming a homogenous medium. In the thorax and abdomen, however, a measurement is mandatory. Using radioactive sources of limited activity the acquisition of a transmission scan of sufficient quality takes about the same time as the emission PET scan itself, and even after the advent of iterative reconstruction methods, noise propagates into the resulting images. Compared to this, a CT scan of the whole body is almost instantaneous, and therefore the hybrid combination of PET/CT which utilizes the CT density information for (almost noise-free) attenuation calculation has made quantitative whole body PET scanning much more feasible. Since its commercial introduction in 2001, the hybrid combination PET/CT has entirely replaced stand-alone PET in clinical use [1, 2]. With the widespread utility of ^{18}F-Fluorodeoxyglucose (FDG)-PET as a practical non-invasive modality for assessing organ function efforts for accurately assessing regional and global metabolic function are imperative. The impact of such measurement is invaluable in the day-to-day practice of medicine. For the purposes of this scientific communication, we have intentionally selected FDG as a model that can be adopted for other PET procedures. There has been significant interest in the recent years for using FDG-PET data in monitoring treatment response in various tumors owing to the several benefits it renders over the anatomic imaging modalities. This further necessitates methods and approaches for more accurate quantification of tumor burden in the entire body. While visual assessment continues to play a pivotal role in the interpretation of PET studies, it is not suitable for being used in clinical trials, where a rigorous and objective measurable parameter is desirable. Calculating SUV at a single time point and assigning standard regions of interest are also clearly inadequate and suboptimal for this purpose.

Since its introduction, PET has been a popular quantitative tool, superior to many other modalities in the functional and structural imaging domains. While the initial dynamic quantitative approaches with FDG-PET intended for calculating absolute glucose metabolic rate in an area of interest (normally in the brain) were reliable, they were technically

*Address correspondence to this author at the Department of Radiology, Division of Nuclear Medicine, Hospital of the University of Pennsylvania, 3400 Spruce Street, 1 Donner Building, Philadelphia, PA 19104-4283, USA; Tel: + 1 215-662-3069; Fax: +1 215-349-5843;
E-mails: Abass.Alavi@uphs.upenn.edu, drsanb@yahoo.com

1573-4056/11 $58.00+.00 ©2011 Bentham Science Publishers Ltd.

demanding and required arterial blood sampling at multiple time points and encompassed complex mathematical procedures [3, 4]. These were, however, found to be impractical for routine use in a busy clinical setting. Quantitative imaging with PET, hence, has undergone constant refinements to develop quantitative methods that would be simple yet reasonably accurate and which could complement visual image interpretation and minimize the inter-observer variability [5].

2. PET DATA ANALYSIS: THE PARAMETERS

The various methods of PET data analysis can be primarily classified into the following three major groups (the latter approach can be divided into 3 categories as shown below):

(i) Qualitative analysis or visual assessment;

(ii) Semi-quantitative analysis which includes standardized uptake value (SUV) and lesion to background ratio (L:B ratio), and

(iii) Absolute quantitative analysis;

(a) Non-linear regression (NLR)

(b) Patlak graphical analysis and derived methods, and

(c) Simplified quantitative methods.

2.1 Quantitative Versus Visual Assessment of FDG Uptake

The uptake in an abnormal focus in a FDG-PET study is the result of "metabolic contrast". Significant inter- and intra-observer variability of PET image interpretation can occur due to the subjective nature of the visual interpretation and has been a source of concern in clinical trials and treatment monitoring where objective assessments are essential. Consequently efforts have been made to define an objective quantitative technique that would be practical and at the same time reasonably accurate.

2.2. Assessment of Absolute Glucose Metabolic Rate

Mathematical compartmental modeling describes the behavior of FDG in various cells and was developed to describe the kinetics of the glucose analogues [^{14}C]-deoxyglucose and FDG in the pioneering work on tracer kinetic modeling [3-4, 6-8]. This kinetic modeling generates the quantitative metabolic rate that can measure FDG metabolism and also yields individual rate constants and thereby provides insight into the various components of glucose metabolism such as transport and phosphorylation. The tracer kinetic modeling of FDG is based upon a standard three-compartment kinetic model originally developed for the brain (Fig. **1**). Compartment 1 (C_1) represents the arterial concentration of free FDG in plasma. It is an "open" compartment exchanging with other tissues in the body that are not measured in the experiment and therefore the "input function" C_1 cannot be predicted within the model, but must be measured separately. For this reason, the name "two tissue compartment model" [9] may be preferred. The first tissue compartment (C_2) represents an extravascular pool of tracer in the tissue, which is available for phosphorylation, and the final compartment (C_3) is the concentration of FDG that has undergone phosphorylation by hexokinase. Dynamic scanning data coupled with rapid arterial blood sampling provide time-activity curves for the specific tumor, organ, or tissue under study. Utilizing non-linear least squares approximations these curves can be fit to obtain the various rate constants. In the mentioned kinetic modeling, the dephosphorylation of FDG-6-phosphate to FDG is generally ignored, although kinetic modeling that includes this reverse process, can lead to more accurate results.

The glucose metabolic rate (MRglu) is calculated by the following equation:

$$\text{MRglu} = \frac{C_p}{LC} \times \frac{K_1 \cdot k_3}{k_2 + k_3} = \frac{C_p}{LC} \times K_i \quad (1)$$

where C_p = plasma glucose concentration, K_1, k_2 = rate constants for forward and reverse transport of FDG, respectively, k_3 = rate of phosphorylation of FDG, K_i = net rate of influx of FDG, and LC = lumped constant relating FDG kinetics to that of glucose. Errors in accurately assessing MRglu, or K_i, include the variance and covariance of the rate constants extracted from the fitting procedure (dependent on the noise in the imaging data), partial volume effects, inaccurate assumptions underlying the model (such as a zero value for k_4), and the contribution from blood pool activity in the imaging data. In addition, the lumped "constant" is actually a slowly varying function of C_p., and only in the brain is it known with some certainty [10-13]. From the initial description in brain imaging [14-15], the methods were subsequently extrapolated into tumor imaging, largely ignoring the unknown *LC*, i.e., focusing directly on FDG uptake as a surrogate measure. The methods described are non-linear regression, Patlak graphical analysis, and Patlak derived methods [16]. These methods (except for the simplified quantitative techniques) all involve dynamic scanning.

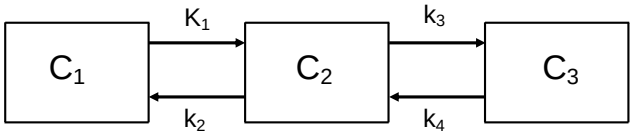

Fig. (1). Kinetic model of FDG behavior. In clinical pharmacology this type of model is traditionally named a "three compartment model" while the usual term within radiotracer modeling today is "two-tissue model" [9]. This emphasizes that C_1 , the concentration of unmetabolized activity in arterial plasma is determined by factors external to the model. C_2 is the concentration of free tracer in the tissue under consideration, and C_3 is concentration of tracer after phosphorylation.

The general advantages of dynamic quantitative approaches include the availability of dynamic data and a low dependency on imaging time. However there are certain disadvantages of dynamic quantitative approaches. They are complex, technically demanding and time consuming procedures; they require a dynamic scanning protocol; there is a need for arterial blood sampling (unless the heart or, during dynamic imaging, a blood-pool structure is in the field of view) to obtain a precise input function [16]. While this is true for brain PET studies, for heart studies such requirements may be easier to accomplish, as the input function can be obtained directly from heart images (left ventricle, aorta, atrium).

In addition, dynamic scanning is a disadvantage in cancer patients with multiple lesions scattered throughout the body. The field of view of the study in dynamic imaging methods like NLR or Patlak-Gjedde analysis is limited to 1 bed position in routine use. Hence, lesions in the specific bed position can be assessed but additional scans are required to assess other lesions that may be evident in a whole body survey.

2.2.1. Non-Linear Regression Analysis

In this method, the net rate of FDG influx (K_i) is estimated from dynamic PET data and from a standard two-tissue compartment model, arterial input function, and non-linear regression analysis [8]. The advantages of this technique are that it is quantitative, independent of uptake period, and provides insight into various rate constants. The usual disadvantages of a dynamic study make its implementation complex.

2.2.2. Patlak–Gjedde Graphical Analysis

In this technique, that was initially described by Patlak [15], the regional concentration at time t after injection can be described by the following equation:

$$c(t) = \lambda \cdot c_p(t) + K_i \int_0^t c_p(\tau)\, d\tau \qquad (2)$$

where

$c(t)$ = activity in the tissue as measured by the PET scanner at time t,

$c_p(t)$ = concentration of FDG in the plasma,

λ= distribution volume of FDG,

K_i = net rate of FDG influx into the tissue, and

τ is a dummy integration variable

The only kinetic assumption is the existence of an irreversible binding compartment. Division on both sides of the equation with the plasma concentration $c_p(t)$ performs a "linearization" which allows K_i to be determined as the slope in a simple plot.

The advantages of this technique include: (i) it is more robust compared to NLR method; (ii) compared to NLR analysis it uses a simplified scanning protocol, avoids noise amplification, and (iii) can generate parametric images. The disadvantages include (i) it still requires dynamic scanning, although not necessarily from the injection, and (ii) compared to NLR analysis, individual rate constants like K_1 and K_3 cannot be obtained.

2.2.3. Simplified Kinetic Methods

The autoradiographic method of Sokoloff (developed for the rat brain) [6, 17] allows a reasonable accurate determination of CMR_{gl} from one static scan, but still requires (arterial) blood sampling from the time of injection to the end of the scan in order to determine the integrated FDG supply to the tissue. The method described by Hunter *et al.* [18] requires only a static scan and a few (venous) blood samples during the scan. These samples are then utilized to scale a population-derived average plasma curve. This method is able to estimate glucose metabolism without the need for a dynamic scan and with a substantially reduced blood sampling protocol. Compared to the SUV method, it takes into account changes in plasma clearance. A potential drawback of this method is that the correction for differences in plasma clearance is only a first-order correction (the peak is assumed to be constant). This method needs to be validated in a large patient population. Sandell *et al.* [19] suggested the use of red blood cells as a "reference" tissue, assuming that the accumulated FDG here can be taken to represent the integral of the input function needed in the autoradiographic method of Sokoloff One potential application would be quantitative studies in children where sampling of the full input curve is an ethical problem.

3. STANDARDIZED UPTAKE VALUE (SUV): POTENTIALS AND PITFALLS

A few synonyms have been used in the literature for SUV: Differential absorption ratio (DAR), differential uptake ratio (DUR), or standardized uptake ratio (SUR).

SUV is the most widely utilized semi-quantitative index in the clinical PET centers across the world. It provides a semi-quantitative measure of FDG metabolism and is defined as the tissue concentration of tracer, as measured by PET (at any given time), divided by the injected dose normalized to patient weight multiplied by a decay factor [20]. It is calculated[1] by dividing the activity concentration in the region of interest (ROI) drawn around the lesion (MBq/mL) by the injected dose (MBq) divided by the body weight (g):

$$SUV = \frac{Mean\ ROI\ concentration\,(MBq/ml)}{Injected\ dose\,(MBq)/Body\ weight\,(g)} \times \frac{1}{decay\ factor\ of\ ^{18}F} \qquad (3)$$

It follows from this definition that if no activity were excreted, a uniform distribution would have the value SUV = 1 (with the approximation of average body density being 1 g/ml). Note also that the activity unit cancels out, showing that as long as the PET scanner is calibrated in units of the dose calibrator actually used for measuring the patient activity, the accuracy of that calibrator does not affect the result. Although dose calibrator measurements ideally should be traceable to national standards, this fact is likely to reduce variability in SUV between centers and over time, compared to "absolute" measurements.

3.1. Advantages and Shortcomings of Simple SUV Measurements

SUV estimation is usually an automated procedure and can be readily calculated with current software supplied with commercial PET scanners. There exists a linear relationship between the SUV and the rate of glucose metabolism as measured by kinetic modeling. Two studies [21, 22] have documented this and registered correlation coefficients of 0.91 and 0.84, respectively. The correlation improves further

[1] Despite the wording in this definition ("as measured by PET" , "in the ROI drawn") we shall assume that there exists an "ideal" SUV, as determined by an ideal PET scanner, to which we compare. Only in this sense is it meaningful to say, e.g., that a measured SUV is underestimated due to resolution or other effects. A similar argument might be used for the timing, but as described we maintain here that SUV is a function of time.

Table 1. Factors Influencing Standardized Uptake Value (SUV) Determination for FDG at Intended Regions of Interest, their Undesirable Effects, and Associated Required Corrective Measures. (Based on Basu *et al.* [95] with permission from Elsevier Inc.)

A. Patient Related Factors

Factor	Effects	Corrective Measures
Body size and habitus (3.3)	SUV in obese patients overestimates FDG uptake relative to normal patients	Use of lean body mass (SUV_{LBM}) or body surface area (SUV_{BSA})
Serum glucose levels (3.4)	Reduced FDG uptake in target tissues with increasing blood glucose levels, i,e, both SUV and FDG are low.	Control of blood glucose before administering FDG and applying correction factor for glucose level
Organ and lesion motion	Reduction of SUV	Respiratory gating or 4D reconstruction

B. Technical Factors

Factor	Effects	Corrective Measures
Duration of uptake period (3.5)	Increase in SUV with increasing time in malignant lesions	Standardization of time of image acquisition
Attenuation correction and reconstruction methods (spatial filter kernel, image resolution, number of iterations)	Underestimation of SUV with highly smoothed reconstruction	Standardize acquisition and reconstruction algorithms
Partial-volume effects (4.1, 4.2)	Underestimation of SUV in lesions with diameters smaller than 2-3 × spatial resolution	Adopt an optimal partial volume correction factor
Size of the ROI and non- uniformity of tracer distribution in the lesion	Low SUV_{mean} for large ROIs and high random errors in smaller ROIs	Standard size ROIs placed reproducibly in the same location, SUV_{max} preferable to SUV_{mean}.
Organ and lesion motion	Mismatch between EM and CT data	Respiratory gating or 4D reconstruction

when body surface area or lean body mass is used for normalization rather than body weight. The SUV method is technically less demanding and computationally simple (with no requirement for blood sampling) and requires considerably less scanner time than the dynamic acquisition protocols. As a result, this method has replaced the more cumbersome dynamic procedures in clinical practice for assessing metabolism in the tumors and other diseases.

3.2. Factors Affecting the Reliability of SUV

The common calibration of scanner and dose calibrator, of course, is essential. Several other factors can affect the reliability of SUV [23]. These can be divided into (i) injection related (ii) patient related, and (iii) technical factors comprising acquisition, reconstruction and evaluation. The description of (ii) and (iii) are detailed in (Table **1**). The injection related factors comprise degree of infiltration of administered FDG dose at the site of injection, residual activity in the syringe and correction for the decay of the injected dose from time of dose measurement to scan, all factors that affect the denominator of eq. (3).

There are many factors that could affect the accuracy of quantification with PET/CT imaging. The most challenging one has been with imaging of thoracic lesions or non-small cell cancer in which respiratory motion could impact the diagnostic and staging accuracy. Misregistration between the CT and PET data due to respiratory motion in the thorax and abdomen was reported soon after commercial introduction of PET/CT and has been one of the most challenging research topics in PET/CT. Fast gantry rotation of less than 1 s per revolution and a large detector coverage of >2 cm enable a CT scan of over 100 cm in the cranial-caudal direction in 20 s. On the other hand, it normally takes 2 to 5 min to acquire the PET data of every 15 cm. The temporal resolutions of CT and PET are very different: less than 1 s for CT and about one respiratory cycle for PET. This mismatch in the temporal resolution may cause a misalignment of the tumor position between the CT and PET data, and may compromise quantification of PET data.

Respiratory gating is another important development in PET/CT for RT. Although, 4D-PET can also be performed on this PET/CT for RT, its application has been limited due to the total acquisition time of approaching 40 min. Most of the patients cannot hold their arms up over their heads for over 30 min and the long acquisition time could induce patient motion and compromise the PET/CT study. Moreover, the statistics of 4D-PET is poor due to splitting-up the coincidence events into multiple bins or phases for 4D-PET, and the spatial resolution of PET in general is only around 5-10 mm. 4D-PET with respiratory gating increases the SUV and improves the consistency of tumor volumes between PET

and CT. In contrast, 4D-CT can be performed in less than 2 min for the coverage of the whole lungs. There is normally high contrast between the lung tumor and the parenchyma except when the lung tumor is connected to a similar tissue density of the mediastinum and chest wall.

3.3. SUV Dependence on Body Habitus

In most current generation PET scanners, the SUV is normalized to patient body weight (designated as SUV_{BW}). However, body habitus may also be important, since adipose tissue typically demonstrates lower FDG uptake compared to other tissues owing to much less metabolic activity. Consequently, in heavier patients with a high fraction of total body fat, SUV overestimates the metabolic activity in non-adipose tissues compared to the situation in patients of normal weight. Studies have investigated the feasibility of correcting SUV with regard to other parameters such as lean body mass (SUV_{LBM}) and body surface area (SUV_{BSA}) and found them to be superior [24-26] compared to $SUV_{BW.}$ The latter corrective methods reduce the variation of SUV related to the patient body composition and habitus. Due to the complex power-dependency of BSA on BW, SUV_{BSA}=1 does not have the same simple interpretation as for SUV_{BW}.

Kim *et al.* [24] examined the value of normalization of SUV with body surface area (SUV_{BSA}) in 44 patients with cancer with body weights ranging from of 45 to 115 kg. They observed a strong positive correlation between SUV_{BW} and body weight but only a weak correlation between SUV_{BSA} and body weight with a near flat regression line. These authors concluded that SUV_{BW} overestimates FDG uptake in large patients and that SUV_{BSA} is preferable over SUV_{BW}. Subsequently two studies have confirmed this observation, and have concluded that SUV_{BSA} was superior to both SUV_{BW} and SUV_{LBM}. Graham *et al*. [27] took this a step further and derived (fitted) a normalization based on a function of BSA and BW (i.e., height and weight), the result of which turned out to be a power function of weight alone. Zasadny *et al.* [28] addressed the same concern by studying the relationship between SUVs in normal tissues and body weight in 28 nondiabetic women with newly diagnosed untreated primary breast cancer with body weights ranging from 45 to 107 kg, and observed a positive correlation between SUV and body weight for liver and spleen metabolic activity. In heavy patients, SUVs for these tissues were up to two times higher than those of the lighter patients. They concluded that correction of SUV for lean body mass (SUV_{LBM}) eliminated the weight dependence of the SUV. Nevertheless, some authors feel that these differences between the normalization methods are small except in very obese patients [29].

3.4. SUV Dependence on Blood Glucose Level

Several studies have demonstrated that SUVs of malignant lesions depend substantially upon the glycemic status. Hyperinsulinemia leads to enhanced glycolysis in adipose tissue and in muscles, and thereby reduce SUV values in other tissues. Note that, unlike in the dependency of body habitus, the reduced SUV here correctly describes a reduced FDG uptake. Most PET centers usually require a maximum plasma glucose level ranging from 150 to 200 mg/dl in patients undergoing FDG-PET studies. Interestingly, Zhuang *et al.* [30] noted that the effects of glucose concentration differ between malignant and inflammatory processes. They observed that elevated blood glucose levels up to 250 mg/dl do not appear to affect the SUV in the inflammatory or other benign lesions.

3.5. SUV Changes Over Time in Malignant and Benign Tissues

Currently most centers employ SUV measurement at a single time point by assigning a standard ROI. It is obvious that variations in the time interval between tracer injection and image acquisition (i.e. FDG uptake period) substantially influence SUV. It must be noted, that due to the duration of the scan itself and its typical composition of a number of axial fields-of-view, a certain time difference within the body is unavoidable. In comparisons of sequential patient scans the effect is minimized by using standard protocols, always scanning in the same direction. Hamberg *et al.* [31] demonstrated that the equilibrium time (no change in concentration of this compound) in bronchial carcinoma varied from 4-6 hours post-injection, and decreased after therapy to 2-3 hours post-injection. These authors concluded that the time interval of 45–60 minutes leads to values of SUV, significantly under the potential maximum because, in most tumors, FDG uptake continues to rise beyond this period, and typically does not reach a plateau for several hours. Lodge *et al.* [32] also noted that in high-grade sarcomas maximal FDG was found at 4 hours whereas such equilibrium was achieved within 30 minutes in benign lesions. Investigators at the University of Pennsylvania, in their study of FDG uptake over extended time periods (over 8 hours) in patients with non small cell lung cancer showed that while tumor sites revealed increased uptake of FDG over 3-4 hours, surrounding normal tissues showed declining values with time. These data indicate that SUV in normal and abnormal tissues change substantially over time and therefore the time interval between the administration and imaging should be taken into consideration in such measurements.

Also, there exists considerable overlap between active inflammatory processes and malignant lesions when SUV is employed for this distinction. Therefore, a threshold value for SUV alone cannot be employed to differentiate between the two. Several approaches have been explored to enhance the specificity of FDG-PET for assessing potential malignant lesions. For example, dual-time point FDG-PET imaging has been utilized in assessing various malignancies including those of the head and neck [33], lung [34], breast [35-37] cervix [38], gallbladder [39], and central nervous system [40]. The theoretical basis for the role of this approach in this setting lies in the fact that dephosphorylation in tumor cells is either absent or very slow compared to that in normal cells due to their low glucose-6-phosphatase content. This results in a build up of contrast between malignant lesions and the normal tissues with time which further increases lesion detectability on delayed images. This approach has been tested by several investigators as a potential way to distinguish malignant from benign lesions.

Hustinx *et al.* [33] examined the utility of dual-time point scanning in 21 patients with head and neck cancer who were scanned serially at two time points, the first at 70 minutes (range 47-112) and the second at 98 minutes (range 77-142)

after the intravenous injection of FDG. The mean interval between emission scans was 28 minutes (range 13-49). SUVs were generated for the cerebellum, tongue, larynx, malignant lesion, and a matched contralateral site. The ratio of tumor SUV to contralateral SUV increased by 23% ± 29% over time whereas this ratio for inflammatory sites increased by only 5% ± 15% (p=0.07). They proposed this approach as a useful means for differentiating malignant lesions from inflammation and non-specific uptake in normal tissues.

Matthies *et al.* [34] investigated this method for the assessment of pulmonary nodules. Thirty six patients with 38 known or suspected malignant pulmonary nodules underwent PET scanning of the thorax at 2 time points: the first was at 70 minutes (range, 56-110) and the second was at 123 minutes (range, 100-163) after the intravenous administration of FDG. In this study, single-time point PET scanning with a threshold SUV of 2.5 (at time point 1) had a sensitivity of 80% and a specificity of 94%, while dual-time point scanning with a threshold value of a 10% increase in SUV between the first and second time points provided a sensitivity of 100% and a specificity of 89%.

Recent studies by Kumar *et al.* [36] and Mavi *et al.* [37] reported high sensitivity, specificity, and accuracy in breast carcinoma with a dual-time point approach. Lesion detectability increased from 83% at 1.5 hour images to 93% at 3 hour images in a study by Boerner *et al.* [35] in breast carcinoma.

Ma *et al.* [38] examined the usefulness of this technique in detecting para-aortic lymph node (PALN) metastases from cervical cancer. These data revealed that an additional scan at 3 hours is helpful for detecting PALN, especially for lower PALN metastases. Nishiyama *et al.* [39] investigated this approach in gallbladder carcinoma and concluded that delayed FDG-PET is more helpful than early FDG-PET for evaluating this cancer. Spence *et al.* [40] applied this method in supratentorial gliomas coupled with kinetic modeling. The estimated k_4 values for tumors were not significantly different from those of cerebral gray matter (GM) in early imaging but were lower at the delayed times. A report by Zhuang *et al.* [41] revealed an increase in SUV on delayed scans in known malignant lesions, whereas the SUVs of benign lung nodules decreased slightly over time. In contrast, the SUVs of the inflammatory lesions caused by radiation therapy and those of the lesions of painful lower limb prostheses remained stable over time. The application of this approach to predict the nature of the bone marrow FDG uptake was studied by Houseni *et al.* [42]. They noted that malignant lesions in the bone marrow result in significantly higher levels of FDG uptake over time than those affected by chemotherapeutic agents.

In many of these studies, the dual-time point approach improved both the sensitivity and the specificity of PET for various malignancies, including breast, lung, and head and neck cancers. This can be explained as follows: increasing FDG uptake over time in the malignant lesions allows differentiating them from benign etiologies with higher specificity, whereas increased lesion-to-background ratio (resulting from a combination of FDG washout from the surrounding normal tissues and enhanced FDG uptake in cancer) leads to higher sensitivity for detecting cancer. This is a noteworthy observation, as there is usually a trade-off between sensitivity and specificity for most other diagnostic tests when a new approach is adopted.

4. FUTURE IMPLICATIONS

In summary, several studies have demonstrated that absolute SUV measurement does not always allow for optimal separation of malignant from benign lesions. Change in SUV over time may prove to be useful for improving the accuracy of FDG-PET imaging for this purpose. Delaying FDG-PET imaging beyond the traditional 1 hour time should also be considered since most lesions show increasing FDG uptake over the time up to several hours. When comparing lesions and in the same lesions noted on images the SUV should be measured at same time point to enhance its reliability.

4.1. Correction of SUV for the Partial Volume Effect (PVE)

The partial volume effect (PVE) is an important factor for measuring the radiotracer concentration with accuracy. This is mostly related to the scanner resolution and is applicable to (homogeneous) objects with sizes less than 2-3 times the spatial resolution of the PET scanner. In addition, physiological and patient motions during data acquisition are also major factors in degrading spatial resolution, thereby also contributing to the PVE. It is important to realize the problems related to internal organ and lesion motion and the actual possibility to account and compensate for it by using 4D respiratory gated (RG) PET/CT acquisition techniques. In fact 4D RG PET/CT can significantly contribute to improve the quantification in PET/CT not only because these techniques allow accounting and compensating for the lesion motion but also because they allow the best spatial and temporal match between PET and CT data to be obtained. This is an important point also for all the dual-point and follow up clinical protocols in order to avoid the attenuation correction errors occuring from possible mismatch caused by organ and lesion motion.

The phenomenon of PVE is akin to what is observed with other imaging techniques including SPECT and structural imaging. Though extensively addressed in brain PET studies [43-49], this is a major source of concern in optimal assessment of malignant lesions [50]. Typically, the best resolution (as measured by laboratory experiments) achieved by the modern generation of clinical whole-body PET scanners is at best 4 mm [51]. However, in clinical practice the actual spatial resolution of the reconstructed images is substantially less than that specified by phantom experiments owing to the limited statistics in the acquired data sets and the limitations of the reconstruction algorithms. This limited spatial resolution does not allow for an accurate measurement of the true SUV in structures and lesions less than 2-3 times the spatial resolution of the PET scanner as defined by the full-width at half-maximum (FWHM) of a point spread function. It is well known that the contrast between the lesion and the surrounding background decreases as the size of the lesion becomes smaller, and may disappear completely beyond a certain point [52]. While many physicians refer to the SUV of 2.5 to discriminate between benign and malignant lung lesions, such a value is well recognized as an arbitrary threshold de-

$$corSUV = \frac{\frac{region's\ activity\ (MBq) - background\ activity\ (MBq)}{lesion's\ size\ on\ CT\ scan\ \ cm^3}}{\frac{Injected\ dose\ (MBq)}{Body\ weight\ (g)}} \quad (4)$$

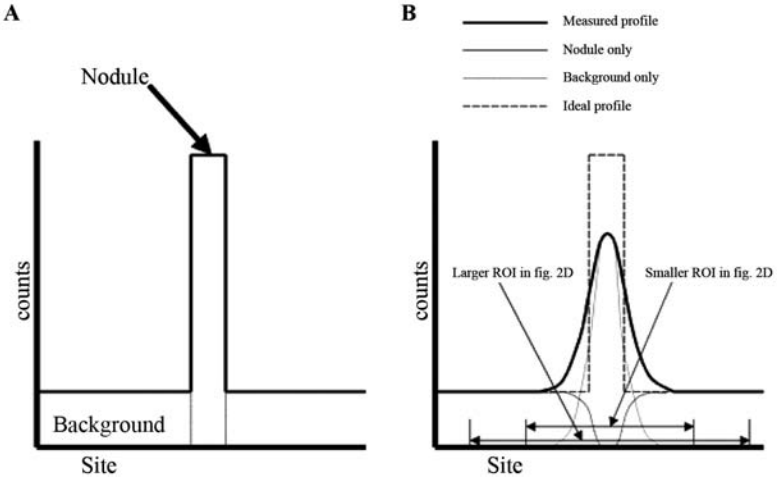

Fig. (2). A. Profile of small lung nodule with uniform FDG uptake using "ideal" PET scanner with perfect spatial resolution; normal lung tissue showing uniformly low FDG activity. **B.** Profile of measured FDG activity with current PET scanner technology through the same nodule in same lung (thick-lined curve). The true distribution of FDG (ideal profile) is indicated by broken line. Note that area under profile assuming the "ideal" PET scanner indicated in A is equal to that using current PET scanner indicated in B. The mentioned fig. 2D (not reproduced here) merely shows the placement of the two circular regions on top of the lung nodule. Reprinted with permission of Springer Science and Business Media from Hickeson *et al*. [54].

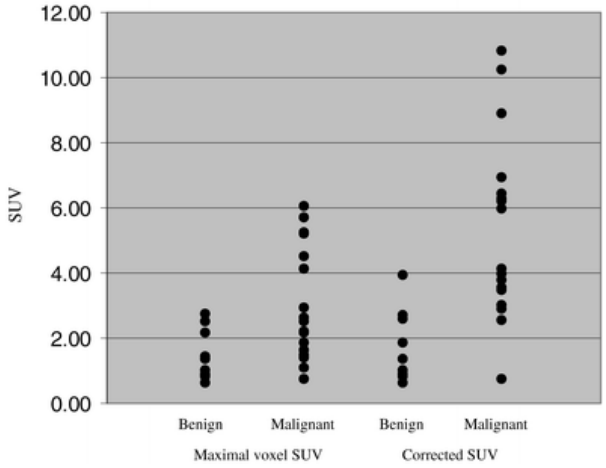

Fig. (3). SUVs of benign and malignant lung lesions measuring equal to or less than 2 cm using uncorrected and corrected maximal voxel determinations. Reprinted with kind permission of Springer Science and Business Media from Hickeson *et al.* [54].

pending on PET scanner used, acquisition parameters and reconstruction algorithm.

Several approaches to minimize PVE have been described. Broadly they can be categorized into three groups based on the underlying principles [53]: (i) methods that correct for resolution losses after reconstruction of images using various models, (ii) methods that incorporate PVE modeling within the reconstruction process and (iii) methods that use the size of the lesion as determined by anatomic imaging data (e.g. CT/MRI) to correct for PVE.

Factors affecting Recovery coefficients (RCs): These include lesion to background (L/B) ratio, matrix size and so on. Furthermore, it should be pointed out that RCs are usually obtained in a static condition (no motion) but are then applied to lesions which most of the time are moving. We shall describe the latter approach in more detail, which is probably the most practical one in the clinical settings.

With partial volume correction, Hickeson *et al.* [54] investigated this effect in the assessment of pulmonary lesions, and noted that there is a significant underestimation of SUV in lesions smaller than 2 cm in size. By correcting the measured value by using lesion size measured from the CT scan (which was assumed to represent the true size of the lesion), improved differentiation between malignant and benign lesions was achieved.

Hickeson *et al.* [54] reported an increase in accuracy from 58% to 89% in the metabolic activity of lung nodules measuring less than 2 cm when a SUV threshold of 2.5 was adopted to distinguish between benign and malignant lesions (Figs. **2–4**). In this study, each lesion's SUV was determined by using two different methods. The maximum voxel SUV was determined in a circular ROI with a diameter of 0.8 cm (two voxels) at the plane with maximal FDG uptake in the lesion. In the second method, the SUV was corrected for underestimation of the true metabolic activity of the entire lesion because of the suboptimal spatial resolution and the PVE. Two ROIs were drawn around the lesion. The smaller of the two included all voxels associated with the lesion. In practice, this was drawn at least 0.8 cm outside the 50% uptake level of the maximum activity to include all of the counts resulting from the solitary pulmonary nodule. The second larger ROI surrounded the smaller ROI as well as its surrounding background. Thus, lesion background could be determined from the average uptake outside the smaller ROI and inside the larger ROI. Note that the halfway point between the maximum lesion activity and the surrounding

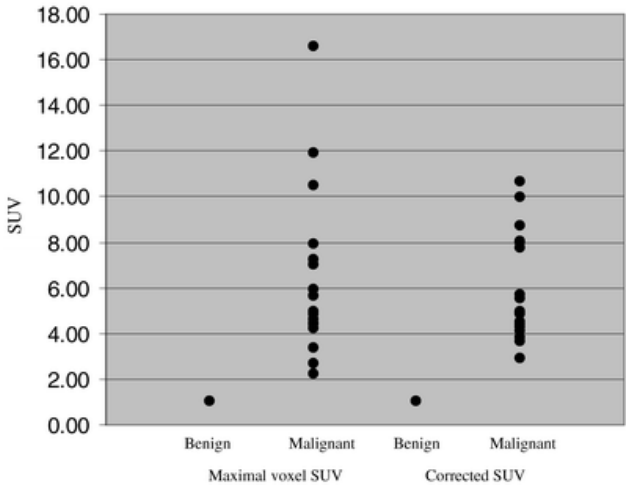

Fig. (4). SUVs of benign and malignant lung lesions measuring more than 2 cm using both methods. Reprinted with kind permission of Springer Science and Business Media from Hickeson *et al.* [54].

background activity is frequently used as the true size of the lesion. The background uptake was then subtracted from the average uptake in the small ROI. Therefore, the corrected SUV was calculated by including the injected dose, the patient's weight, and time after injection by using the following formula:

$$corSUV = \frac{\frac{region's\ activity\ (MBq) - background\ activity\ (MBq)}{lesion's\ size\ on\ CT\ scan\ \left(cm^3\right)}}{\frac{Injected\ dose\ (MBq)}{Body\ weight\ (g)}} \quad (4)$$

Avril *et al.* [29] examined the role of a similar approach in breast cancer, and noted that correction of SUV for the PVE and normalization for blood glucose level yielded the highest diagnostic accuracy among several PET quantitative procedures. Lubberink *et al.* [55] compared the results of ^{110m}In-DTPA-D-Phe^1-octreotide PET images with those of the ^{111}In-DTPA-D-Phe^1-octreotide SPECT scans, and observed that partial volume correction greatly improved detection of small tumors and allowed accurate quantitation of tracer concentration in lesions of various sizes (Fig. **5**). From these studies, it is clear that PVE correction is crucial in the measurement of tumor FDG uptake in the small lesions. It is of importance when monitoring response to therapeutic intervention, where the reduction in the size of a tumor could result in underestimation of the true concentration of compounds such as FDG in the intended sites. It should be noted, that inhomogeneities in a large tumour may still cause the reported SUV_{max} to be too low, even if the overall size of the tumour exceeds 3 times the scanner FWHM.

4.2. Applications of PVE Correction in Neurology

Correction for partial volume correction was studied already in the 1980s when CT and low resolution PET instruments were utilized to examine patients with Alzheimer's disease (AD) and other central nervous system disorders that usually result in cerebral atrophy [43]. This technique was later investigated by using modern segmentation methodologies and high resolution MR imaging [56, 57]. The latter has allowed for accurate measurement of gray matter (GM) and white matter (WM) as well as cerebral spinal fluid (CSF) volumes in the brain [58, 59].

Kohn *et al.* [58] described a new computerized system developed to process standard spin-echo magnetic resonance imaging data for estimation of brain parenchyma and cere-

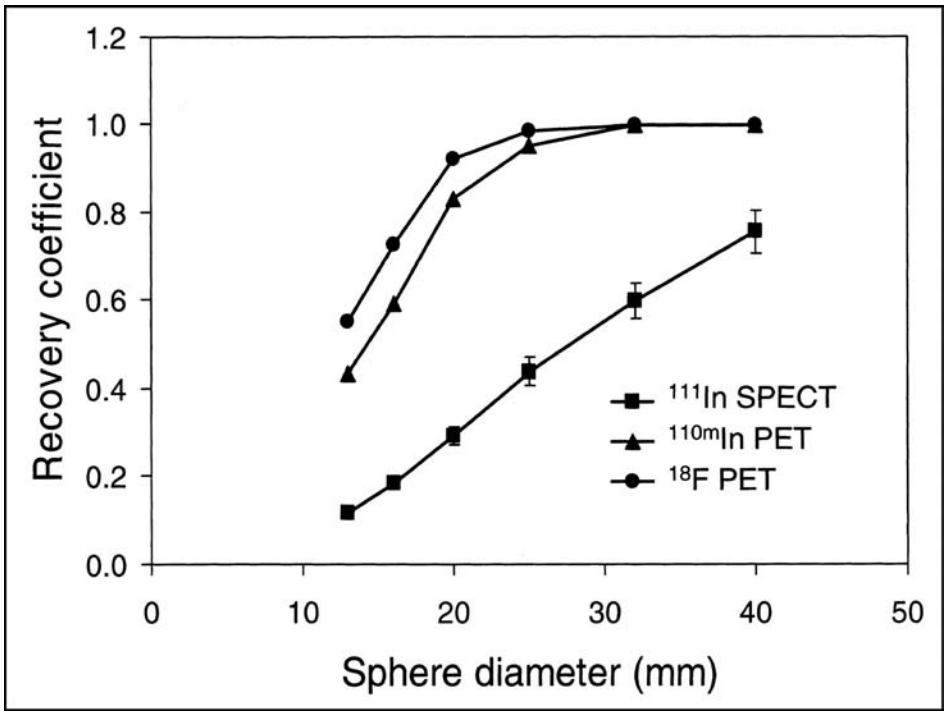

Fig. (5). Sphere recovery functions for partial volume correction for ^{110m}In-PET, ^{111}In-SPECT, and ^{18}F FDG-PET. Reprinted by permission of the Society of Nuclear Medicine from Lubberink *et al.* [55].

brospinal fluid volumes. In phantom experiments, these estimated volumes corresponded closely to the true volumes (r = .998), with a mean error less than 1.0 cm^3 (for phantom volumes ranging from 5-35 cm^3), with excellent intra- and inter-observer reliability. In a clinical validation study with actual brain images of 10 human subjects, the average coefficient of variation among observers for the measurement of absolute brain and CSF volumes was 1.2% and 6.4%, respectively. The intraclass correlation for three expert operators was found to be greater than 0.99 in the measurement of brain and ventricular volumes and greater than 0.94 for total CSF volume. The authors concluded that their technique to analyze MR images of the brain performed with acceptable levels of accuracy, and concluded that it can be used to measure brain and CSF volumes for clinical research. This technique, they believed, could be helpful in the correlation of neuroanatomic measurements to behavioral and physiological parameters in neuropsychiatric disorders.

Tanna *et al.* [44] adopted this computerized segmentation technique in a retrospective analysis of digitized T2-weighted MR images of 16 healthy elderly control subjects and 16 patients with AD. They quantified ventricular and extraventricular CSF and studied the effects of aging and AD on brain function as determined by FDG-PET. In both groups, the degree of atrophy as measured by these techniques was used to correct for metabolic rates obtained by PET. Patients with AD had higher total; extraventricular, total ventricular, and third ventricular CSF volumes (49%, 37%, 99%, and 74%, respectively), and 7% lower brain volumes than the control group. Patients with AD also showed a more marked decline in brain volumes and a greater increase in CSF volumes with advancing age than the control group. The patient group had a 25.0% increase in corrected whole-brain metabolic rates compared to the control group who had only a 15.8% increase by applying the partial volume correction factors. The use of this technique, they concluded, could provide a basis for further studies of aging and dementia, by calculating the accurate rates of regional metabolism of structural components in these settings.

Bural *et al.* [60] studied the effects of a novel quantitative MR imaging segmentation scheme which allows for actual SUV (instead of metabolic rates as reported by Tanna *et al.* as referenced above) calculation of the regional GM, WM, and CSF volumes. This approach resulted in overcoming the difficulties associated with conventional low resolution imaging techniques for measuring actual metabolic activity of the GM. These investigators calculated the volumes of GM, WM, and CSF by using a special segmentation technique on the MR images. This was followed by computation of the mean SUV representing the whole metabolic activity of the brain from the FDG-PET images. They also measured the WM SUV from the upper transaxial slices (centrum semiovale) of the FDG-PET images. The volumes of the GM, WM, and CSF were summed to calculate whole brain volume to enable calculation of global cerebral metabolic activity by multiplying the mean SUV by the total brain volume. Similarly, the whole brain WM metabolic activity was measured by multiplying the mean SUV for the WM by the WM volume. CSF metabolic activity was considered to be 0. Thus, by subtracting the global WM metabolic activity from that of the whole brain, they were able to measure the global GM metabolic activity alone. Finally, by dividing GM global metabolic activity by GM volume, an accurate SUV for GM alone was determined. The brain volumes ranged between 1100-1546 cm^3. The mean SUV for total brain was 4.8-7. Global cerebral metabolic activity of the brain ranged from 5565-9566 SUV-cm^3. The mean SUV for WM was 2.8-4.1. Based on these measurements, they reported that the GM SUV in the sample examined ranged from 8.7-11.3.

5. CONCEPT OF GLOBAL METABOLIC ACTIVITY. ASSESSMENT IN HEALTHY AND DISEASED STATES

The basic principle of derivation of the global metabolic activity is based upon multiplying partial volume corrected average standardized uptake value to the volume of the organ of interest obtained from the CT/MRI. With the introduction of fusion imaging in the day-to-day practice of medicine, we believe, a quantitative approach imbibing data from both structural and functional modalities will be the way forward for accurate assessment of various pathophysiological processes. Medical image segmentation is an integral part of this promising approach by which identification of objects of interest in a given multidimensional image enable us to assess the regional functional parameters of an individual component within an organ. The future impact of this approach is discussed along with a brief overview of the concepts that allow for segmentation of various structural components of different organs. The direct and the most promising impact of this will certainly be in monitoring therapeutic efficacy in several malignancies and incorporation of quantitative FDG-PET data into the different tumor response evaluation scales used in clinical oncology trials like the WHO criteria, the Southwest Oncology Group (SWOG) criteria or the Response Evaluation Criteria in Solid Tumours (RECIST). While the major use of such measurement will be more accurate assessment of disease activity in cancer, which we have termed as "metabolic burden", there are several potential applications as well like the assessment of global metabolic activity in various neuropsychiatric disorders and quantification of atherosclerosis (termed as "atheroburden").

5.1. Principle and Method of Global Metabolic Activity Estimation

The concept of global metabolic activity was first introduced by Alavi *et al.* [3] in assessment of the brain in patients with Alzheimer's disease (AD) and in age-matched controls. These investigators were able to demonstrate that by multiplying segmented brain volumes as determined from MR images by the measured mean cerebral metabolic rates for glucose, significant differences between these two populations can be demonstrated. The same investigators have proposed adopting a similar approach for assessing global normal organ function and overall disease activity in other settings [4].

This concept would require calculating tissue volume by utilizing modern computer based algorithms and accurate (partial volume corrected) measurement of metabolic activities (or other functional process) at each site of interest. The partial volume effect (PVE) is one of the important limiting

Table 2. Whole Brain PET data for AD and Controls. (Adapted with Permission from [96])

	CMRGlc (uncorrected) (mean±S.D.)	CMRGlc (corrected) (mean±S.D.)	Atrophy weighted total brain metabolism (mean±S.D.)	Absolute whole brain metabolism (mean±S.D.)
AD patients	3.15±0.83**	3.91±1.02^{ns}	29.96±7.90***	37.24±9.65*
Controls	3.83±0.70	4.43±0.87	39.09±7.02	45.09±8.52

Cerebral metabolic rate of glucose (CMRGlc) in mg glucose/100 cc brain tissue/min; Atrophy weighted total brain metabolism in mg glucose/brain/min; Absolute whole brain metabolism Absolute whole brain metabolism in mg glucose/brain/min.
P-values refer to comparison with control subjects: ^{ns}: not significant; * <0.02; **< 0.01; *** < 0.001

Table 3. Recovered Whole Brain PET Data for AD and Controls. (Adapted with Permission from [96])

	Recovered CMRGlc (uncorrected) (mean±S.D.)	CMRGlc (corrected) (mean±S.D.)	Atrophy-weighted total brain metabolism (mean±S.D.)	Absolute whole brain metabolism (mean±S.D.)
AD patients	4.89±1.22*	6.06±1.48**	46.61±12.24***	57.86±14.89****
Controls	5.38±0.88	6.22±1.07	55.23±9.82	63.73±10.07

Cerebral metabolic rate for glucose (CMRGlc) in mg glucose/100cc/brain tissue/min; Atrophy weighted total brain metabolism in mg glucose/brain/min; Absolute whole brain metabolism Absolute whole brain metabolism in mg glucose/brain/min.

*Not Significantly different from controls p=0.17

** Not Significantly different from controls p=0.72

***Significantly different from controls p=0.026

****Significantly different from controls p=0.18

technical factors for accurate quantitation with PET and recent advances have made it feasible to correct for partial volume effects on low spatial resolution functional imaging techniques. By multiplying partial volume corrected metabolic measures (such as SUV, rates of metabolism, etc.) by volumetric measures from structural images to yield the metabolic volumetric product (MVP) for the organ of interest or the diseased site, it would be feasible to calculate the global function in the intended tissues. By combining these measurements in the entire body for various pathological states, one can calculate the global metabolic activity of the underlying process.

5.2. Advantages Over the "Structural Data Only" Approach

The power of this concept stems from its ability to rely upon both structural and functional alterations that take place as a consequence of normal processes such as aging or disease states. This is important, as it is well documented that existing uni-dimensional measurement (RECIST) criteria, a standard ROI based SUV, or other semi-quantitative measurements are often prone to inaccuracy and high variability in their generated results [63].

This concept is particularly applicable to cancer both at the initial stage and following treatment. The use of this approach may prove to be essential for testing new therapeutic agents. Similarly, this approach can be effectively employed in other states such as atherosclerosis, cardiac disorders, and central nervous system diseases. Below, we present some data generated based on these concepts.

5.3. Applications of Global Metabolic Activity in Neurology

One of the major domains of neurology where assessment of global metabolic activity is of great interest is that of neuropsychiatric disorders. In order to elucidate the relationship between reduced cognitive function and cerebral metabolism in patients with AD, Basu *et al.* [61] hypothesized that the absolute amount of glucose used by the entire brain would prove to be a more reliable indicator of disease than metabolic rates calculated for a unit of brain weight alone. They investigated 20 patients with the probable diagnosis of AD and 17 age-matched controls who underwent FDG-PET imaging and MR imaging within a few days of each other. The uncorrected cerebral metabolic rate for glucose (CMRGlc) values were atrophy corrected using the following equation:

$$\text{Atrophy corrected average CMRGlc} = \frac{\text{Mean CMRGlc}}{\text{percentage of brain tissue in the intracranial volume}} \quad (5)$$

Absolute whole brain metabolism was calculated by using the formula:

$$\text{Absolute whole brain metabolism} = \text{Atrophy corrected mean CMRGlc} \times \text{brain volume} \quad (6)$$

Average metabolic rates, when corrected for atrophy, were 3.91 ± 1.02 and 4.43 ± 0.87 (mg of glucose per 100 cm^3 brain tissue per minute) for AD patients and controls, respectively. Two other indices were determined as well: atrophy-weighted total brain metabolism (calculated by multiplying the brain volume, determined from MR image analysis, by the average metabolic rate) and absolute whole brain metabolism (calculated by multiplying the brain volume by the average metabolic rate corrected for atrophy). The former showed a very significant difference between the two groups (29.96 ± 7.90 for AD patients compared to 39.1 ± 7.0 for controls, $p < 0.001$). Atrophy-weighted total brain metabolism also correlated with mini-mental status examination (MMSE) scores ($r = 0.59$, $p < 0.01$). Absolute whole brain metabolism was found to be significantly different between

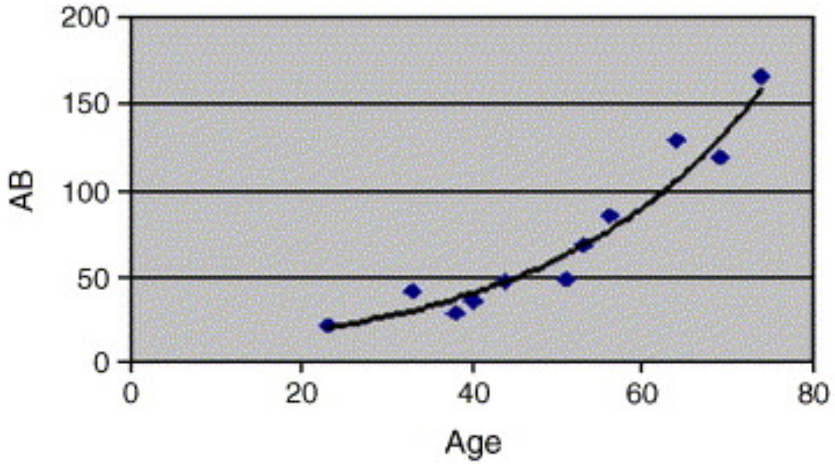

Fig. (6). Assessment of changes in global metabolic activity of aortic atherosclerosis (atheroburden) with increasing age. (Adapted with permission from [60]).

AD and control groups and correlated well with MMSE scores. These data demonstrated that although the metabolic rate per unit weight of the brain is unchanged in AD compared to controls, atrophy-weighted total brain metabolism and absolute whole brain metabolism are significantly affected. They concluded that both indices could prove to be sensitive correlates for cognitive dysfunction in AD (Table **2** and **3**).

5.4. Application of Global Metabolic Activity for Quantitation of Atherosclerosis

Bural *et al.* [60] described a technique for quantifying the extent of atherosclerosis in the aorta by multiplying SUVs in the aortic wall with aortic wall volumetric data provided by CT to yield MVPs. They examined this approach in 18 patients who had both FDG-PET and contrast-enhanced CT of the chest and abdomen. All had homogeneous diffuse FDG uptake in all segments of the aortic wall. The patients were divided into three groups according to their age and FDG uptake was measured in different segments of the aorta by calculating the mean SUV for each segment. On each axial CT image, ROI tracings along the inner and outer wall contours of the aorta were generated. The inner surface area was subtracted from the outer surface area, and net area values for each segment were subsequently multiplied by slice thickness to calculate aortic wall volume. By multiplying SUV by the wall volume, they were able to calculate the atherosclerotic burden (AB) (a special instance of the MVP) for each segment of the aorta. They then compared the aortic wall volumes, SUVs, and AB values in each arterial segment for each age group. When the aortic wall volumes, SUVs, and AB values in each aortic segment for each age group were compared, AB values, SUVs, and wall volumes were found to increase with age ($p<.05$) (Fig. **6**).

5.5. Application of Global Metabolic Activity to Diffuse Hepatic Steatosis

Bural *et al.* [62] adopted this approach to compare the FDG uptake in liver and hepatic MVPs between normal subjects and subjects with diffuse hepatic steatosis by using FDG-PET and MR imaging. They investigated 24 subjects in this study (11 men, 13 women, age range 21-75 years). All subjects had FDG-PET and MR scans within a time interval of 52 ± 60 days. Twelve of the 24 subjects had the diffuse hepatic steatosis based on MR imaging criteria. The remaining twelve were selected as age-matched subjects, as they had normal appearing livers on MR images and on FDG-PET scans. They calculated the mean and maximum hepatic SUVs for both groups for every subject from the FDG-PET images. They also calculated the volume of the liver for each subject from MR images by summing the surface area values and multiplying by slice thickness. Subsequently, the hepatic MVP was calculated by multiplying liver volume by the mean hepatic SUV in each subject. The mean and maximum hepatic SUVs and the hepatic MVPs were compared for two groups. Mean and maximum hepatic SUVs for the group with diffuse hepatic steatosis were 2.2 ± 0.1 and 3.2 ± 0.4, respectively, and 1.8 ± 0.2 and 2.4 ± 0.3 for the control group, respectively, which were all statistically significantly different ($p<0.05$). Hepatic MVP for the group with diffuse hepatic steatosis was 3.7 ± 0.2 (SUV - L), and 2.3 ± 0.9 (SUV - L) for the control group, which were statistically significantly different ($p<0.05$).

5.6. Application of Global Metabolic Activity in Oncology

The concept of whole body metabolic burden (WBMB) has been examined in relation to disease activity in lymphoma patients [63]. Individual lesion metabolic burden (MB) was calculated by measuring the volume on CT (V_{CT}), the mean SUV measured on PET of the CT volume (SUV_{meanCT}), and the Recovery Coefficient (RC):

$$MB = SUV_{meanCT}\left(V_{CT}\right)/RC \qquad (7)$$

where *RC* recovers counts that extend beyond the CT volume due to partial volume effects, and was obtained from a calibration plot study of hot sphere activity within a warm background phantom for the PET scanner used. For lesions > 3 cm, *RC* was 1. The preliminary results showed that MB is a useful measure when corrected for partial volume effects and operator error in drawing ROIs. The WBMB was defined as the sum of the individual metabolic burden of all lesions identified. This index appeared promising to monitor changes in total body tumor burden in patients undergoing treatment.

$WBMB = \sum_{i=1}^{n} MB_i$ where n is the number of individual tumors outlined. Akin to single lesion MB, the WBMB had units of SUV – volume.

More recently, Larson *et al.* [64] proposed the concept of "Total Lesion Glycolysis" (TLG) which was defined as $TLG = SUV_{mean} \times volume\ of\ PET\ lesion$. They further defined the response index (also known as Larson-Ginsberg Index – LGI) as:

$$\Delta TLG\ (LGI) = \frac{\left[(SUV_{mean})_1 \times (Vol)_1 - (SUV_{mean})_2 \times (Vol)_2 \right]}{(SUV_{mean})_1 \times (Vol)_1} \times 100 \quad (8)$$

where "1" and "2" denote the pre- and post-treatment FDG-PET scans, respectively. They investigated a group of 41 locally advanced lung (n=2), rectal (n=17), esophageal (n=16) and gastric (n=6) cancers. They concluded that the visual response score and ΔTLG are substantially correlated with other response parameters and are highly reproducible.

6. IMAGE SEGMENTATION IN QUANTITATIVE PET IMAGING

Image segmentation is defined as the process of classifying the voxels of an image into set of distinct classes. Medical image segmentation has been a popular and challenging area of research. Despite the known limitations, several image segmentation approaches have been proposed and used in the clinical setting including thresholding, region growing, classifiers, clustering, edge detection, Markov random field models, artificial neural networks, deformable models, atlas-guided and many other approaches [65].

Within the context of quantitative PET imaging, image segmentation has found numerous clinical and research applications [5]. This includes estimation of organ volumes or tumor volumes as well as definition of target treatment volumes in radiation therapy [66, 67] or for assessment of treatment response [68, 69], extraction of parameters of clinical relevance such as the left ventricular region in nuclear cardiology [70, 71], automated ROI delineation of structures of interest in dynamic functional imaging [72], generation of functional images to highlight regions of similar temporal behavior (components) [73, 74], determination of the attenuation map in emission tomography [75], anatomically-tomically-guided image reconstruction and partial volume segmentation [48], and construction of voxel-based anthropomorphic phantoms based on high resolution anatomical images. For the latter, the interested reader is refered to a recent review describing the development of such computational models in connection with Monte Carlo modeling tools in radiological sciences [76].

One example (Fig. **7**) of the application of image segmentation shows a representative slice of a clinical T2-weighted MR image through the brain and the corresponding segmentation results separately showing each tissue class (GM, WM, CSF). MR images were first corrected for inhomogeneity and were subsequently intensity standardized before applying a segmentation method on them. The mean intensity and standard deviation for each of GM, WM, and CSF regions are then estimated from the training data set and are fixed once for all. A fuzzy connectedness framework was utilized for creating a brain intracranial mask, and the fuzzy membership value of each voxel in each brain tissue was estimated, and final segmentation of the brain tissues was simply performed via a maximum likelihood criterion as described by Zhuge *et al.* [59].

Another example involves segmentation of the lung parenchyma. Historically, segmentation of the lungs on CT scans was a popular research subject given its usefulness in computer-based analysis of thoracic CT images and computer-aided diagnosis. As a consequence, plenty of image segmentation approaches were proposed and many of them found applications in clinical settings. For example, the software system 3DVIEWNIX [77] was used to segment the CT image of the lungs to obtain the left and the right lung. The steps were as follows: (i) The *Threshold* operation was used to segment the lung tissue from the rest of the CT image. (ii) Subsequently, *Interactive2D* was used to manually remove the areas that were not a part of the lungs or were a part of the airway tree. (iii) The mask that was produced covered the lung area only. Using *Interactive2D* once again, the left lung was removed and hence the mask for the right lung was obtained. (iv) *Algebra* was used to obtain the left lung by subtracting the right lung mask from the entire lung mask. Fig. (**8**) displays the segmentation results on a chest CT in one subject.

To enhance lesion detectability, the use of similarity measures for analysis of dynamic oncological imaging to enhance the contrast between normal tissues and lesions is an appealing approach that needs to be investigated further

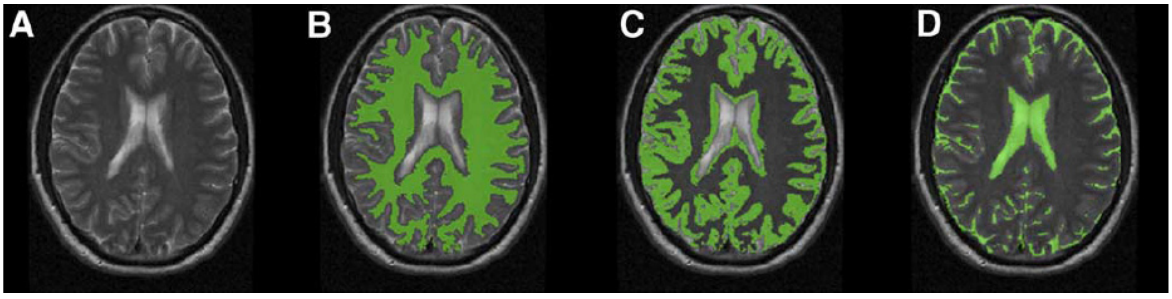

Fig. (7). Segmentation technique used to calculate standard uptake value (SUV) in gray (GM) and white (WM) matter, and cerebrospinal fluid (CSF). **A.** Axial slice of intensity inhomogeneity corrected and intensity standardized T2-weighted image. **B-D**, Color overlays on same axial T2-weighted image corresponding to segmented WM, GM, and CSF, respectively. (Reprinted with permission from [61]).

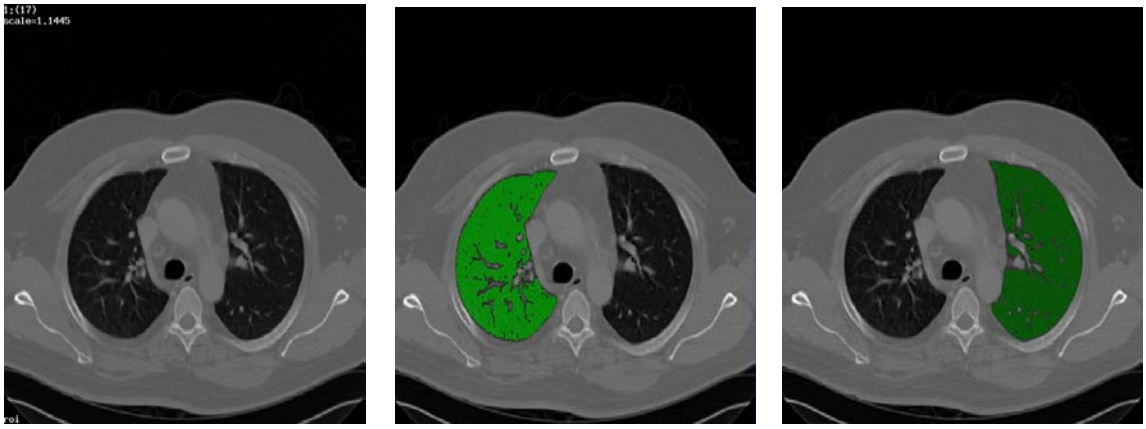

Fig. (8). Illustration of lung CT segmentation results. From left to right: original axial CT image, right lung segmentation, and left lung segmentation. (Reprinted with permission from [61]).

[78]. One such technique, proposed originally for cardiac imaging but could also be applied in oncological PET studies, uses the cross-ψ_B-energy operator, a nonlinear similarity measure which quantifies the interaction between two time-signals including their first and second derivatives [74]. Similarity measure between the time activity curve (TAC) of each pixel and the mean value of the TACs of a reference region of the dynamic image series is calculated, thereby generating images demonstrating temporal changes in radioactive tracer distribution.

As far as partial volume correction is concerned, the accuracy of algorithms depends in part on the degree of accuracy in the segmentation of the anatomical images and the coregistration of anatomical images with the PET data. These effects have been investigated extensively in the literature for both the voxel-based and region-based partial volume correction strategies [47, 49, 79]. It was demonstrated that errors in the segmentation procedure have greater impact but are relatively limited to the mis-segmented region [49]. Overall, it appears that the success of the segmentation of the structural information provided by MR images, for instance, has a higher impact on the accuracy of the corrected estimates [47], compared to the influence of image co-registration, although some authors recently suggested that mis-registration errors have the strongest impact on data accuracy and precision [79]. Notwithstanding, it was suggested that in the absence of major sources of registration or segmentation errors, recovered activity concentration estimates have been found to be typically within 5-10% of true tracer concentration with a standard deviation of a few percent in both phantom and simulation studies [49, 79]. An important development that can be exploited for future simultaneous PET/MR imaging technology dedicated for brain research [80] is to combine various MR imaging segmentation methodologies for both partial volume correction and attenuation compensation [81, 82].

7. NOVEL IMAGE SEGMENTATION APPROACHES IN IMAGE GUIDED RADIATION THERAPY

Within the realm of oncological PET imaging, image segmentation is vital for a variety of specific applications for tumor quantitation in staging, assessment of tumor response to therapy, and definition of target volumes in radiation therapy treatment planning [67, 83]. One of the most difficult issues facing PET-based radiation therapy treatment planning is the accurate delineation of target regions from typical noisy functional images. The major problems encountered in functional volume quantitation are image segmentation and imperfect system response function.

At present, various methods are used in practice to delineate PET–based target volumes [84]. The manual delineation of target volumes using different window level settings and look up tables is the most common and widely used technique in the clinic. However, the method is highly operator-dependent and is subject to high variability between operators. Semi-or fully-automated delineation techniques might offer several advantages over manual techniques by reducing operator error/subjectivity, thereby improving reproducibility. There have been remarkable progress in automated image segmentation during the last few years and the performance validation in a clinical setting is now under way. It is imperative that the application of these findings into routine treatment planning scenario would help define viable tumor boundaries with better precision.

One such novel automated system for the segmentation of oncological PET data aiming at providing an accurate quantitative analysis tool was recently proposed [85]. The initial step involves Expectation Maximization (EM)-based mixture modeling using a k-means clustering procedure, which varies voxel order for initialization. A multiscale Markov model is then used to refine this segmentation by modeling spatial correlations between neighboring image voxels. Anthropomorphic phantom experiments were conducted for quantitative evaluation of the performance of the proposed segmentation algorithm**.** The comparison of actual tumor volumes to the volumes calculated using different segmentation methodologies including standard k-means, spatial domain Markov Random Field Model (MRFM), and the new multiscale MRFM showed that the latter dramatically reduces the relative error. The analysis of the resulting segmentations of clinical oncologic PET data seems to confirm that this methodology can successfully segment patient lesions. Another promising technique using the Markov chain model was recently proposed by Hatt *et al.* who modified their original algorithm into fuzzy locally adaptive Bay-

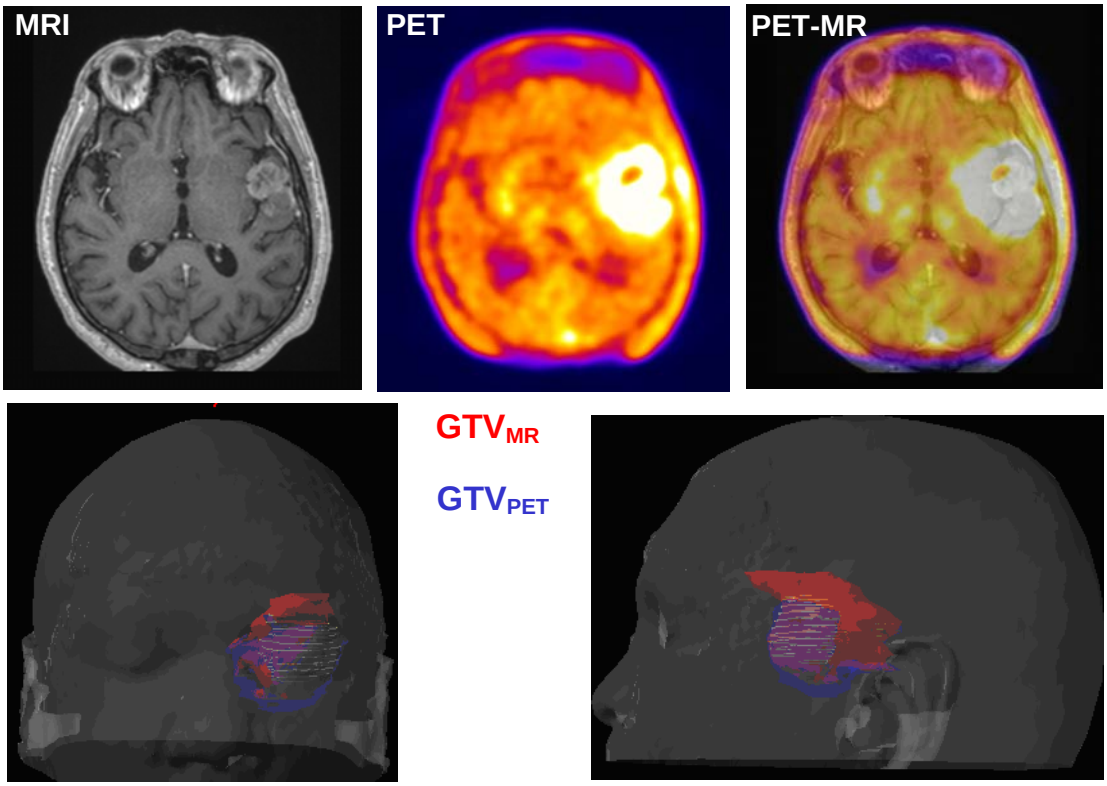

Fig. (9). Typical example of geographical mismatch between gross tumor volumes (GTVs) defined on MRI and PET in a patient with a glioblastoma. Top: from left to right, Gadolinium enhanced T1-weighted MRI, corresponding ^{18}F-FET PET study, and fused PET/MR. Bottom: 3-D reconstructions illustrating the substantial mismatch. Note that the GTV defined on MRI overestimates the tumour extension compared with GTV defined on PET images. Adapted with permission from [87] and [97].

esian (FLAB) to improve segmentation of small lesions [86]. This Bayesian approach uses adaptive estimation of priors using a family of distributions from the Pearson's system.

Vees *et al.* [87] compared various image segmentation techniques in the delineation of gross tumor volume (GTV) in patients with cerebral glioma (Fig. **9**). The study results highlighted the limitations associated with some of the segmentation algorithms (e.g. 2.5 standardized uptake values cutoff and the gradient finding GTV approaches) compared to the signal-to-background ratio (SBR)-based adaptive thresholding technique and its impact on RT planning in patients of cerebral glioma. The authors concluded the selection of the most appropriate FET-PET based segmentation algorithm is crucial for correct delineation of resulting GTV [87].

A recent study compared nine PET image segmentation techniques [88]. These include manual delineation performed by an experienced radiation oncologist on both the CT (CT_{man}) and PET (PET_{man}) images, four semi-automated methods comprising the Signal-to-Background Ratio (SBR)-based adaptive thresholding technique [89], region growing (RG) [90], Black *et al.* technique [91], Nestlé *et al.* technique [92], and three fully automated methods: standard fuzzy C-means (FCM) [93], the spatial FCM (FCM-S) which incorporates nonlinear anisotropic diffusion filtering thus allowing the integration of spatial contextual information and the wavelet-based FCM-S algorithm (FCM-SW) which also considers inhomogeneity of tracer uptake through the use of the à trou wavelet transform [94]. Representative segmentation results of FDG PET/CT image of a patient presenting with histologically proven non-small cell lung cancer are shown in Fig. (**10**). The GTVs defined on the non-homogeneous lesion using 9 segmentation techniques are depicted on both the CT (left) and FDG-PET (right) transaxial slices.

8. CONCLUSIONS

The appearance of hybrid PET/CT scanners have created a unique possibility for quantitative measurements of physiological and patophysiological processes in the human body, and for precisely correlating these with anatomy. The development of software methods to register to other modalities, e.g. MR has further strenghtened the use of PET.

The power of accurate quantitative assessment of global disease activity in patients may certainly have several advantages over measuring SUV_{max} in one index lesion. This concept is particularly applicable to cancer both at the initial stage and following treatment to estimate the metabolic burden of the disease and may be essential for testing new therapeutic agents. Similarly, this approach can be effectively employed in other disease states such as atherosclerosis, hepatic and cardiac disorders. Sophisticated quantitative analysis methodologies are likely to become widely available in clinical settings and not just limited to PET research facilities with advanced scientific and technical support. This will enhance the potential of PET-CT imaging to "personalize" treatment by evaluating the effectiveness of therapy and to recognize ineffective treatments, which may also be costly

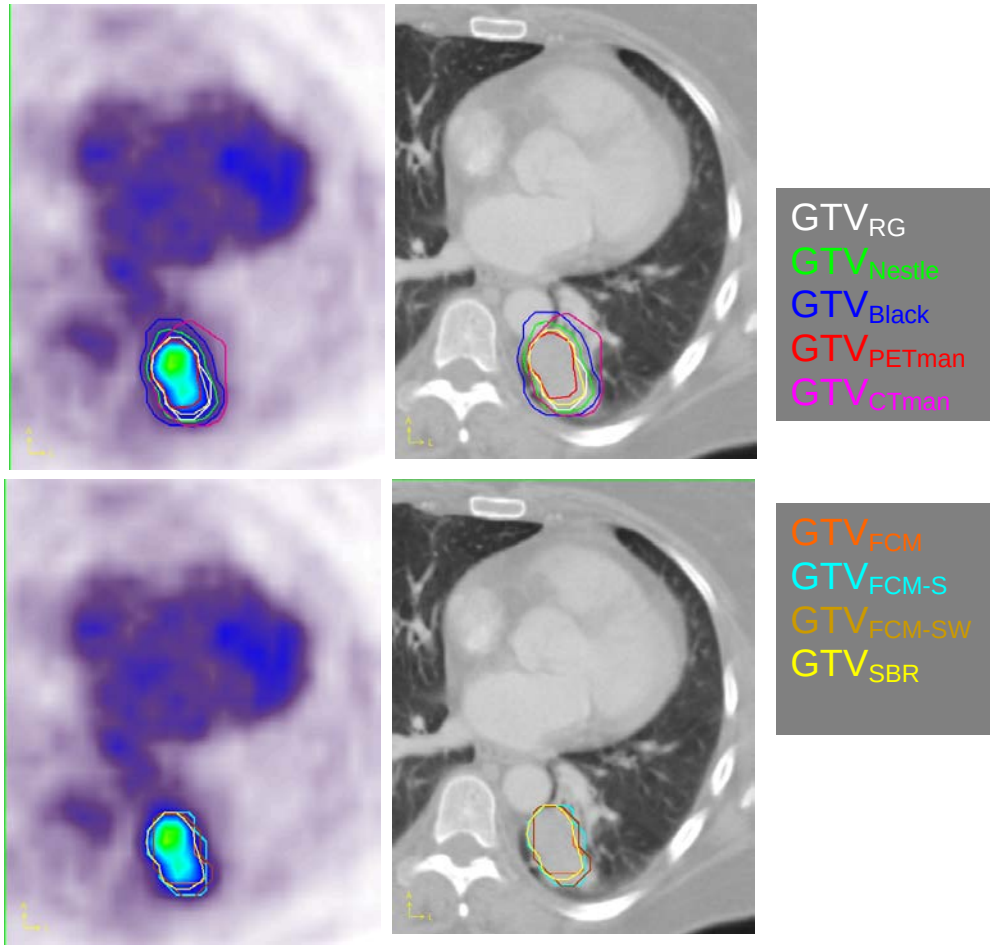

Fig. (10). Representative segmentation results of FDG PET/CT image of a patient presenting with histologically proven non-small-cell lung cancer. The gross tumor volumes defined on the ellipsoidal homogeneous lesion using 9 segmentation techniques are depicted on both the CT (left) and FDG-PET (right) transaxial slices. These include manual delineation performed by an experienced radiation oncologist on both the CT (CT_{man}) and PET (PET_{man}) images, 4 semi-automated methods comprising the Signal-to-Background Ratio (SBR)-based adaptive thresholding technique [89], region growing (RG) [90], Black et al. technique [91], Nestlé *et al.* technique [92], and 3 fully automated methods: standard fuzzy C-means (FCM) [93], the spatial FCM (FCM-S) which incorporates nonlinear anisotropic diffusion filtering to incorporate information about the spatial context and the wavelet-based FCM-S algorithm (FCM-SW) which also considers inhomogeneity of tracer uptake through the use of the à trou wavelet transform [94].

or risky. Thus further refinements might prove invaluable for the optimal utilization of this powerful imaging technology.

ACKNOWLEDGEMENTS

This work was in part supported by the Swiss National Science Foundation under grants SNSF 31003A-125246, 33CM30-124114, and Geneva Cancer League.

(Adapted in part from Basu S, Zaidi H, Houseni M, Bural G, Udupa J, Acton P, Torigian DA, Alavi A. Novel quantitative techniques for assessing regional and global function and structure based on modern imaging modalities: implications for normal variation, aging and diseased states. Semin Nucl Med 2007; 37(3): 223-39; S. Basu, H. Zaidi, A. Alavi. Clinical and research applications of quantitative PET imaging. *PET Clinics of North America*. *Volume 2, Issue 2, Pages 161-172;* S. Basu, H. Zaidi, A. Alavi. New concepts for assessing global organ function and disease activity based on combined PET and structural imaging techniques. *PET Clinics of North America*. *Volume 2, Issue 2, Pages 279-287).*

ABBREVIATIONS

(C)MRGlc	=	(cerebral) metabolic rate of glucose
CT	=	computed tomography
FDG	=	Fluorodeoxyglucose
MRI	=	Magnetic Resonance Imaging
MVP	=	metabolic volumetric product
NLR	=	Non-linear regression
SUV	=	standardized uptake value
PVE	=	partial volume effect
TLG	=	Total Lesion Glycolysis

REFERENCES

[1] Kinahan PE, Townsend DW, Beyer T, Sashin D. Attenuation correction for a combined 3D PET/CT scanner. Med Phys 1998; 25: 2046-53.

[2] Beyer T, Townsend DW, Brun T, *et al.* A combined PET/CT scanner for clinical oncology. J Nucl Med 2000; 41: 1369-79.

[3] Alavi A, Reivich M, Greenberg J, *et al*. Mapping of functional activity in brain with 18F-fluoro-deoxyglucose. Semin Nucl Med 1981; 11: 24-31.

[4] Reivich M, Alavi A, Wolf A, *et al*. Use of 2-deoxy-D[1-11C]glucose for the determination of local cerebral glucose metabolism in humans: variation within and between subjects. J Cereb Blood Flow Metab 1982; 2: 307-19.

[5] Zaidi H, editor. Quantitative analysis in nuclear medicine imaging. New York: Springer; 2006.

[6] Sokoloff L, Reivich M, Kennedy C, *et al*. The [^{14}C]deoxyglucose method for the measurement of local cerebral glucose utilization: theory, procedure, and normal values in the conscious and anesthetized albino rat. J Neurochem 1977; 28: 897-916.

[7] Reivich M, Kuhl D, Wolf A, *et al*. The [18F]fluorodeoxyglucose method for the measurement of local cerebral glucose utilization in man. Circ Res 1979; 44: 127-37.

[8] Phelps ME, Huang SC, Hoffman EJ, Selin C, Sokoloff L, Kuhl DE. Tomographic measurement of local cerebral glucose metabolic rate in humans with (F-18)2-fluoro-2-deoxy-D-glucose: validation of method. Ann Neurol 1979; 6: 371-88.

[9] Innis RB, Cunningham VJ, Delforge J *et al*. Consensus nomenclature for in vivo imaging of reversibly binding radioligands. J Cereb Blood Flow metabol 2007; 27: 1533-1539.

[10] Hasselbalch SG, Madsen PL, Knudsen GM, Holm S, Paulson OB. Calculation of the FDG lumped constant by simultaneous measurement of global glucose and FDG metabolism in humans. J Cereb Blood Flow metabol 1998; 18: 154-160.

[11] Hasselbalch SG, Holm S, Pedersen HS, *et al*. The F-18 FDG lumped constant determined in human brain from extraction fractions of FDG and glucose. J Cereb Blood Flow metabol 2001; 21: 995-1002.

[12] Graham MM, Muzi M, Spence AM. The FDG lumped constant in normal human brain**.** J Nucl Med 2002; 43: 1157-66.

[13] Wu HM, Bergsneider M, Glenn TC, *et al*. Measurement of the global lumped constant for FDG in normal human brain. Mol Imaging Biol 2003; 5: 32-41.

[14] Gjedde A. Calculation of cerebral glucose phosphorylation from brain uptake of glucose analogs in vivo: A re-examination. Brain Res Rev1982; 4: 237-74.

[15] Patlak CS, Blasberg RG, Fenstermacher JD. Graphical evaluation of blood-to-brain transfer constants from multiple-time uptake data. J Cereb Blood Flow Metab 1983; 3: 1-7.

[16] Carson R. Tracer kinetic modeling in PET. In: Valk PE, Bailey DL, Townsend DW, Maisey MN, editors. Positron Emission Tomography: Basic Science and Clinical Practice. Chapter 4 ed. London: Springer-Verlag; 2003; 147-79.

[17] Schmidt KC, Lucignani G, Sokoloff L. Fluorine-18-fluorodeoxyclucose PET to determine regional cerebral glucose utilization: A reexamination. J Nucl Med 1996; 37: 394-399.

[18] Hunter G, Hamberg L, Alpert N, Choi N, Fischman A. Simplified measurement of deoxyglucose utilization rate. J Nucl Med 1996; 37: 950-5.

[19] Sandell A, Ohlsson T, Erlandsson K, Strand SE. An alternative method to normalize clinical FDG studies. J Nucl Med 1998; 39: 552-5.

[20] Huang S-C. Anatomy of SUV. Nucl Med Biol 2000; 27: 643-6.

[21] Minn H, Leskinen-Kallio S, Lindholm P, Bergman J, Ruotsalainen U, Teras M, *et al*. [18F]fluorodeoxyglucose uptake in tumors: kinetic vs. steady-state methods with reference to plasma insulin. J Comput Assist Tomogr 1993; 17: 115-23.

[22] Kole A, Nieweg O, Pruim J, *et al*. Standardized uptake value and quantification of metabolism for breast cancer imagin with FDG and L-[1-11C]tyrosine PET. J Nuc Med 1997; 38: 692-6.

[23] Keyes J. SUV: Standard Uptake Value or Silly useless Value? J Nucl Med.1995; 36: 1836-9.

[24] Kim CK, Gupta N, Chandramouli B, Alavi A. Stardized uptake values of FDG: body surface area correction is preferable to body weight correction. J Nucl Med 1994; 35: 164-7.

[25] Kim CK, Gupta N. Dependency of standardized uptake values of fluorine-18 fluorodeoxyglucose on body size: Comparison of body surface area correction and lean body mass correction. Nucl Med Commun1996;17: 890-4.

[26] Gupta N, Frank A, Dewan N, *et al*. Solitary pulmonary nodules: detection of malignancy with PET with 2-[F-18]-fluoro-2-deoxy-D-glucose. Radiology 1992; 184: 441-4.

[27] Graham MM, Peterson LM, Hayward RM. Comparison of simplified quantitative analyses of FDG uptake. Nucl Med Biol 2000; 27: 647-55.

[28] Zasadny KR, Wahl RL. Standardized uptake values of normal tissues at PET with 2-[fluorine-18]-fluoro-2-deoxy-D-glucose: variations with body weight and a method for correction. Radiology 1993; 189: 847-50.

[29] Avril N, Bense S, Ziegler SI, *et al*. Breast imaging with fluorine-18-FDG PET: quantitative image analysis. J Nucl Med 1997; 38: 1186-91.

[30] Zhuang HM, Cortes-Blanco A, Pourdehnad M, *et al*. Do high glucose levels have differential effect on FDG uptake in inflammatory and malignant disorders? Nucl Med Commun 2001; 22: 1123-8.

[31] Hamberg LM, Hunter GJ, Alpert NM, Choi NC, Babich JW, Fischman AJ. The dose uptake ratio as an index of glucose metabolism: useful parameter or oversimplification? J Nucl Med 1994; 35: 1308-12.

[32] Lodge M, Lucas J, Marsden P, Cronin B, O'Doherty M, Smith M. A PET study of (18)FDG uptake in soft tissue masses. Eur J Nucl Med 1999; 26: 22-30.

[33] Hustinx R, Smith RJ, Benard F, *et al*. Dual time point fluorine-18 fluorodeoxyglucose positron emission tomography: a potential method to differentiate malignancy from inflammation and normal tissue in the head and neck. Eur J Nucl Med 1999; 26: 1345-8.

[34] Matthies A, Hickeson M, Cuchiara A, Alavi A. Dual time point 18F-FDG PET for the evaluation of pulmonary nodules. J Nucl Med 2002; 43: 871-5.

[35] Boerner AR, Weckesser M, Herzog H, *et al*. Optimal scan time for fluorine-18 fluorodeoxyglucose positron emission tomography in breast cancer. Eur J Nucl Med 1999; 26: 226-30.

[36] Kumar R, Loving VA, Chauhan A, Zhuang H, Mitchell S, Alavi A. Potential of dual-time-point imaging to improve breast cancer diagnosis with 18F-FDG PET. J Nucl Med 2005; 46: 1819-24.

[37] Mavi A, Urhan M, Yu JQ, *et al*. Dual time point 18F-FDG PET imaging detects breast cancer with high sensitivity and correlates well with histologic subtypes. J Nucl Med 2006; 47: 1440-6.

[38] Ma SY, See LC, Lai CH, *et al*. Delayed (18)F-FDG PET for detection of paraaortic lymph node metastases in cervical cancer patients. J Nucl Med 2003; 44: 1775-83.

[39] Nishiyama Y, Yamamoto Y, Fukunaga K, *et al*. Dual-time-point 18F-FDG PET for the evaluation of gallbladder carcinoma. J Nucl Med 2006; 47: 633-8.

[40] Spence AM, Muzi M, Mankoff DA, *et al*. 18F-FDG PET of gliomas at delayed intervals: Improved distinction between tumor and normal gray matter. J Nucl Med 2004; 45:1653-9.

[41] Zhuang H, Pourdehnad M, Lambright ES, *et al*. Dual time point 18F-FDG PET imaging for differentiating malignant from inflammatory processes. J Nucl Med 2001; 42: 1412-7.

[42] Houseni M, Chamroonrat W, Bural G, *et al*. Alavi A. Promising role of dual time FDG-PET imaging in assessing focal and diffuse bone marrow disorders. J Nuc Med 2006; 47: 227P.

[43] Chawluk J, Alavi A, Dann R, *et al*. Positron emission tomography in aging and dementia: effect of cerebral atrophy. J Nucl Med 1987; 28: 431-7.

[44] Tanna NK, Kohn MI, Horwich DN, *et al*. Analysis of brain and cerebrospinal fluid volumes with MR imaging: impact on PET data correction for atrophy. Part II. Aging and Alzheimer dementia. Radiology. 1991; 178: 123-30.

[45] Rousset OG, Ma Y, Evans AC. Correction for partial volume effects in PET: principle and validation. J Nucl Med 1998; 39: 904-11.

[46] Aston JA, Cunningham VJ, Asselin MC, Hammers A, Evans AC, Gunn RN. Positron emission tomography partial volume correction: estimation and algorithms. J Cereb Blood Flow Metab 2002; 22: 1019-34.

[47] Quarantelli M, Berkouk K, Prinster A, *et al*. Integrated software for the analysis of brain PET/SPECT studies with partial-volume-effect correction. J Nucl Med2004; 45: 192-201.

[48] Baete K, Nuyts J, Laere KV, *et al*. Evaluation of anatomy based reconstruction for partial volume correction in brain FDG-PET. NeuroImage 2004; 23: 305-17.

[49] Zaidi H, Ruest T, Schoenahl F, Montandon M-L. Comparative evaluation of statistical brain MR image segmentation algorithms and their impact on partial volume effect correction in PET. Neuroimage 2006; 32: 1591-607.

[50] Soret M, Bacharach SL, Buvat I. Partial-volume effect in PET tumor imaging. J Nucl Med 2007; 48: 932-45.
[51] Zaidi H, Alavi A. Current trends in PET and combined (PET/CT and PET/MR) systems design. PET Clinics 2007; 2: 109-23.
[52] Weber W, Young C, Abdel-Dayem HM, *et al*. Assessment of pulmonary lesions with 18F-fluorodeoxyglucose positron imaging using coincidence mode gamma cameras. J Nucl Med 1999; 40: 574-8.
[53] Rousset O, Rahmim A, Alavi A, Zaidi H. Partial volume correction strategies in PET. PET Clinics 2007; 2: 235-49.
[54] Hickeson M, Yun M, Matthies A, *et al*. Use of a corrected standardized uptake value based on the lesion size on CT permits accurate characterization of lung nodules on FDG-PET. Eur J Nucl Med Mol Imaging 2002; 29: 1639-47.
[55] Lubberink M, Tolmachev V, Widstrom C, Bruskin A, Lundqvist H, Westlin JE. 110mIn-DTPA-D-Phe1-octreotide for imaging of neuroendocrine tumors with PET. J Nucl Med 2002; 43: 1391-7.
[56] Muller-Gartner HW, Links JM, Prince JL, *et al*. Measurement of radiotracer concentration in brain gray matter using positron emission tomography: MRI-based correction for partial volume effects. J Cereb Blood Flow Metab 1992; 12: 571-83.
[57] Meltzer CC, Zubieta JK, Links JM, Brakeman P, Stumpf MJ, Frost JJ. MR-based correction of brain PET measurements for heterogeneous gray matter radioactivity distribution. J Cereb Blood Flow Metab 1996; 16: 650-8.
[58] Kohn MI, Tanna NK, Herman GT, *et al*. Analysis of brain and cerebrospinal fluid volumes with MR imaging. Part I. Methods, reliability, and validation. Radiology 1991; 178: 115-22.
[59] Zhuge Y, Liu J, Udupa JK, Membership-based multiprotocol MR brain image segmentation. Medical Imaging 2003: Image Processing; 2003 2003/05/16/; San Diego, CA, USA. vol. 5032; pp 1572-9.
[60] Bural GG, Torigian DA, Chamroonrat W, *et al*. Quantitative assessment of the atherosclerotic burden of the aorta by combined FDG-PET and CT image analysis: a new concept. Nucl Med Biol 2006; 33: 1037-43.
[61] Basu S, Zaidi H, Houseni M, *et al*. Novel quantitative techniques for assessing regional and global function and structure based on modern imaging modalities: Implications for normal variation, aging and diseased states. Sem Nucl Med 2007; 37: 223-39.
[62] Bural G, Torigian D, Burke A, *et al*. Quantitative assessment of the hepatic metabolic volume product in patients with diffuse hepatic steatosis and normal controls through use of FDG-PET and MR imaging: A novel concept. Mol Imaging Biol 2009; 12: 233-9.
[63] Berkowitz A, Basu S, Srinivas S, Sankaran S, Schuster S, Alavi A. Determination of whole-body metabolic burden as a quantitative measure of disease activity in lymphoma: a novel approach with fluorodeoxyglucose-PET. Nucl Med Commun 2008; 29: 521-6.
[64] Larson SM, Erdi Y, Akhurst T, *et al*. Tumor treatment response based on visual and quantitative changes in global tumor glycolysis using PET-FDG imaging. The visual response score and the change in total lesion glycolysis. Clin Positron Imaging 1999; 2: 159-71.
[65] Pham DL, Xu C, Prince JL. A survey of currents methods in medical image segmentation. Annual Reviews 2000; 2: 315-37.
[66] van Baardwijk A, Baumert BG, Bosmans G, van Kroonenburgh M, Stroobants S, Gregoire V, *et al*. The current status of FDG-PET in tumour volume definition in radiotherapy treatment planning. Cancer Treat Rev 2006; 32: 245-60.
[67] Zaidi H, Vees H, Wissmeyer M. Molecular PET/CT imaging-guided radiation therapy treatment planning. Acad Radiol 2009; 16: 1108-33.
[68] Francis RJ, Byrne MJ, van der Schaaf AA, *et al*. Early prediction of response to chemotherapy and survival in malignant pleural mesothelioma using a novel semiautomated 3-dimensional volume-based analysis of serial 18F-FDG PET scans. J Nucl Med 2007; 48: 1449-58.
[69] Green A, Francis R, Baig S, Begent R. Semiautomatic volume of interest drawing for 18F-FDG image analysis - method and preliminary results. Eur J Nuc Med Mol Imaging [10.1007/s00259-007-0602-3]. 2008; 35: 393-406.
[70] Behloul F, Lelieveldt BP, Boudraa A, Janier MF, Revel D, Reiber JH. Neuro-fuzzy systems for computer-aided myocardial viability assessment. IEEE Trans Med Imaging 2001; 20:1302-13.
[71] Slomka PJ, Radau P, Hurwitz GA, Dey D. Automated three-dimensional quantification of myocardial perfusion and brain SPECT. Comput Med Imaging Graph 2001; 25: 153-64.
[72] Wong K-P, Dagan F, Meikle SR, Fulham MJ. Segmentation of dynamic PET images using cluster analysis. IEEE Trans Nucl Sci 2002; 49: 200-7.
[73] Bentourkia Mh. A flexible image segmentation prior to parametric estimation. Comput Med Imaging Graph 2001; 25: 501-6.
[74] Boudraa A, Cexus J-C, Zaidi H. Functional segmentation of dynamic nuclear medicine images by cross-PsiB energy operator. Comput Meth Prog Biomed 2006; 84: 148-54.
[75] Zaidi H, Hasegawa BH. Determination of the attenuation map in emission tomography. J Nucl Med 2003; 44: 291-315.
[76] Zaidi H, Xu XG. Computational anthropomorphic models of the human anatomy: The path to realistic Monte Carlo modeling in medical imaging. Annu Rev Biomed Eng 2007; 9: 471-500.
[77] Udupa JK, Odhner D, Samarasekera S, *et al*. 3DVIEWNIX: an open, transportable, multidimensional, multimodality, multiparametric imaging software system. Medical Imaging 1994: Image Capture, Formatting, and Display; 1994 1994/05/01/; Newport Beach, CA, USA. vol. 2164; pp. 58-73.
[78] Thireou T, Kontaxakis G, Strauss LG, Dimitrakopoulou-Strauss A, Pavlopoulos S, Santos A. Feasibility study of the use of similarity maps in the evaluation of oncological dynamic positron emission tomography images. Med Biol Eng Comput 2005; 43: 23-32.'
[79] Frouin V, Comtat C, Reilhac A, Gregoire M-C. Correction of partial volume effect for PET striatal imaging: fast implementation and study of robustness. J Nucl Med 2002; 43: 1715-26.
[80] Schlemmer HP, Pichler BJ, Schmand M, *et al.* Simultaneous MR/PET imaging of the human brain: feasibility study. Radiology 2008; 248: 1028-35.
[81] Zaidi H. Is MRI-guided attenuation correction a viable option for dual-modality PET/MR imaging? Radiology 2007; 244: 639-42.
[82] Hofmann M, Pichler B, Schölkopf B, Beyer T. Towards quantitative PET/MRI: a review of MR-based attenuation correction techniques. Eur J Nuc Med Mol Imaging 2009; 36: 93-104.
[83] Paulino AC, Thorstad WL, Fox T. Role of fusion in radiotherapy treatment planning. Semin Nucl Med 2003; 33: 238-43.
[84] Zaidi H, El Naqa I. PET-guided delineation of radiation therapy treatment volumes: A survey of image segmentation techniques. 2010; 37: 2165-87.
[85] Montgomery D, Amira A, Zaidi H. Fully automated segmentation of oncological PET volumes using a combined multiscale and statistical model. Med Phys 2007; 34: 722-36.
[86] Hatt M, Cheze le Rest C, Turzo A, Roux C, Visvikis D. A fuzzy locally adaptive Bayesian segmentation approach for volume determination in PET. IEEE Trans Med Imaging 2009; 28: 881-93.
[87] Vees H, Senthamizhchelvan S, Miralbell R, Weber D, Ratib O, Zaidi H. Assessment of various strategies for 18F-FET PET-guided delineation of target volumes in high-grade glioma patients. Eur J Nucl Med Mol Imaging 2009; 36: 182-93.
[88] Belhassen S, Llina Fuentes CS, Dekker A, De Ruysscher D, Ratib O, Zaidi H. Comparative methods for 18F-FDG PET-based delineation of target volumes in non-small-cell lung cancer [abstract]. J Nucl Med 2009; 50:27P.
[89] Daisne JF, Sibomana M, Bol A, Doumont T, Lonneux M, Gregoire V. Tri-dimensional automatic segmentation of PET volumes based on measured source-to-background ratios: influence of reconstruction algorithms. Radiother Oncol 2003; 69: 247-50.
[90] Graves EE, Quon A, Loo BW, Jr. RT_Image: an open-source tool for investigating PET in radiation oncology. Technol Cancer Res Treat 2007; 6: 111-21.
[91] Black QC, Grills IS, Kestin LL, *et al*. Defining a radiotherapy target with positron emission tomography. Int J Radiat Oncol Biol Phys 2004; 60: 1272-82.
[92] Nestle U, Kremp S, Schaefer-Schuler A, S *et al*. Comparison of different methods for delineation of 18F-FDG PET-positive tissue for target volume definition in radiotherapy of patients with non-Small cell lung cancer. J Nucl Med 2005; 46: 1342-8.
[93] Boudraa AE, Champier J, Cinotti L, Bordet JC, Lavenne F, Mallet JJ. Delineation and quantitation of brain lesions by fuzzy clustering in positron emission tomography. Comput Med Imaging Graph 1996; 20: 31-41.
[94] Belhassen S, Zaidi H "A novel fuzzy C-means algorithm for unsupervised heterogeneous tumor quantification in PET" Med Phys 2010; 37: 1309-24.
[95] Basu S, Alavi A. Defining co-related parameters between 'metabolic' flare and 'clinical', 'biochemical', and 'osteoblastic' flare and

establishing guidelines for assessing response to treatment in cancer. Eur J Nucl Med Mol Imaging 2006; 34: 441-3.

[96] Alavi A, Newberg AB, Souder E, Berlin JA. Quantitative analysis of PET and MRI data in normal aging and Alzheimer's disease: atrophy weighted total brain metabolism and absolute whole brain metabolism as reliable discriminators. J Nucl Med 1993; 34: 1681-7.

[97] Weber DC, Zilli T, Buchegger F, *et al*. [(18)F]Fluoroethyltyrosine-positron emission tomography-guided radiotherapy for high-grade glioma. Radiat Oncol 2008; 3:44.

Received: March 20, 2010 Revised: June 14, 2010 Accepted: February 20, 2011